Initial Upsurge of BMPs Enhances Long-Term Osteogenesis in *in-vitro* Bone Regeneration

Krishna Kundu, Sharad V. Jaswandkar, Dinesh R. Katti, and Kalpana S. Katti*

Department of Civil Construction and Environmental Engineering

North Dakota State University, Fargo ND 58108, USA

* Author to whom all correspondences should be addressed

Kalpana.katti@ndsu.edu , Ph: 701-231-9504

Abstract

Recent challenges in repair of critical size bone defects necessitates the need for scaffolds with accelerated bone defect repair. The higher surface area, complex porous architecture, and appropriate mechanical properties offered by engineered interlocking block scaffolds enables their use as bone grafts for critical size defect repair. Here, an interlocking scaffold system is designed by incorporating the bone morphogenic proteins (BMP-2 and BMP-7) and co-culturing with human osteoblasts (hFOB) and mesenchymal stem cells (MSCs). The complete release of BMPs from the porous scaffolds is observed by day 16. We evaluate the long-term effect of BMPs on *in vitro* bone regeneration at 9 weeks. A significant increase in the bone-related proteins and osteogenesis-related Wnt-factors with BMPs coated samples is observed as compared to uncoated samples, indicating that BMPs played an essential role in initial osteogenesis and ECM formation. We also report significant increase in the mineralized bone nodules with BMPs coated samples compared to without BMPs samples, suggesting that BMPs play a crucial role in mineralized ECM formation. Furthermore, nanoindentation results demonstrate a 120% increase in the elastic modulus at nine weeks with BMPs coated scaffolds indicating enhanced ECM formation. Thus, BMPs play a crucial role in osteogenesis at the initial stages and the effect of BMPs persists beyond the timescale of complete release at 16 days. This study provides valuable insight into the mechanisms of the BMPs association with bone tissue formation and demonstrates the feasibility of the interlocking scaffold system as a bone graft for bone defect repair application.

Statement of Significance

BMP-2 and BMP-7 are highly regarded as potent growth factors used for large bone defect repair and can be used with porous scaffolds. It is unclear how and what role BMPs play over a long period of time for bone defect therapies. Here, for the first time, we examined the change in the nanomechanical properties of the newly formed bony tissue over nine weeks and report a 120% increase in the elastic modulus at nine weeks with BMP coated scaffolds. In addition, alizarin Red S staining images and gene expression results suggest that BMPs play a significant role in mineralized ECM formation and influence osteogenesis initiation. This work provides a deeper understanding of the mechanisms of the BMPs association with bone tissue formation.

Key words: Biomaterials, nanoindentation, Bone morphogenic protein, bone tissue engineering, scaffolds

1. Introduction

Bone is a highly vascularized and dynamic natural nanocomposite that is constantly remodeled throughout an individual's lifespan. Every year, more than 170 million new bone fractures occur worldwide, making it the second most transplanted tissue after blood[1-3]. In contrast to other tissues and organs, bone tissue usually has better self-healing ability. The damaged part can regain its original structure and mechanical strength without leaving fibrotic scars. However, when the range of bone defects exceeds the critical-size defect (CSD), bone defects cannot heal by themselves and require reasonable clinical intervention[4] and the fracture does not heal and forms a nonunion. Every year, roughly 100,000 cases of bone fractures in the United States result in nonunion[5, 6]. Nonunion can be caused by various factors, including bone tumor removal, previous radiation treatment, infection, and trauma which are common issues in

clinical treatment[7]. Because of the extent of the defect and disturbance in the usual processes that allow osteogenesis and angiogenesis, the bone defect does not heal properly. Mechanical fixation to prevent movement of bone at the defect site and to conduct bone autogenous bone grafting is currently one of the existing standards of care for the treatment of a critical-size bone defect[8]. However, this strategy involves surgeries at multiple anatomic sites and is linked with higher risks of infection-related complications and pain. One alternate treatment involves bone transport surgery[9], which is highly stressful and painful for individuals and can take several months for recovery. Biomaterials-based procedures offer an alternative to traditional bone grafting.

Bone regeneration is a complex process involving various growth factors, including bone morphogenetic proteins (BMPs), vascular endothelial growth factor (VEGF), insulin-like growth factor (IGF), and a few others[10]. Among these, BMPs are the most important osteogenic growth factors shown to induce bone formation by inducing mesenchymal stem cells (MSCs) toward osteoblastic differentiation[11]. The BMPs are multi-functional growth factors that play a vital role in embryonic development and adult homeostasis by morphogenesis, differentiation, proliferation, and apoptosis of various types of cells in the body. BMPs also promote angiogenesis by prompting osteoblasts to produce VEGF[12]. BMPs are mostly known for cartilage and bone formation. In 1965, Urist reported that bioactive components in the demineralized bone matrix induce bone formation[13]. BMPs signaling occurs through both canonical Smad-dependent pathways (BMP ligands, receptors, and Smads) and non-canonical Smad-independent signaling pathways (p38 mitogen-activated protein kinase pathway, MAPK). Both canonical Smad-dependent pathways and non-canonical Smad-independent signaling pathways express Runx2 gene expression to control osteogenesis[14-16].

For the treatment of the non-unions, BMPs are considered a favorable approach because they are considered the most potent toward bone regeneration[17]. There are fifteen different BMPs are found in mammals; among them, rhBMP-2 and rhBMP-7 are FDA approved. BMP-2 and BMP-7 have been tested in several preclinical studies showing the ability to induce bone regeneration[18-20] and evaluated in clinical trials to treat various bone disorders such as non-unions, open fractures, and osteonecrosis[21-25]. Clinical trials results suggested that BMP-2 and BMP-7 are safe, significantly reduced the frequency of bone grafting procedures and effective in non-union bone defect[21, 24, 26].

The Wnt and bone morphogenic protein (BMP) signaling pathways are important for many biological events and complement each other for bone regeneration[27]. BMP-2 induces Wnt and activates the β-catenin signaling pathway during endochondral ossification, and the β-catenin signaling pathway regulates the early phases of chondrogenesis and osteogenesis[28]. BMP-2 promotes osteogenic differentiation by increasing the expression of LRP-5 and stabilizing β-catenin through the downregulation of β-Trcp[29, 30]. A substantial reduction of osteogenesis occurs with β-catenin deficiency. The function of BMP-2 toward bone formation is inhibited by DKK-1 overexpression[28, 31, 32]. Overall, the Wnt/ β-catenin pathway is found to be very crucial for osteogenesis and bone mass formation along with BMP signaling pathway.

3D porous scaffolds with the appropriate mechanical properties are required for bone tissue engineering[33, 34]. The scaffolds serve as mechanical support during tissue growth, and their porous structure provides nutrient supply and helps waste removal[35]. Biocompatible polymers reinforced with hydroxyapatite (HAP) are extensively used in bone tissue engineering because of the similar compositions of the mineral phase of the bone[36]. HAP enhanced cell attachment, cell proliferation, and osteogenic differentiation of stem cells[37, 38]. Inorganic fillers are also used to

improve the mechanical properties of the scaffold to facilitate bone tissue formation[39]. Montmorillonite (MMT) nano-clay is used as an inorganic filler to enhance the mechanical properties of the scaffold[40]. Along with the mechanical properties of the scaffold, MMT nano-clay also improves cell adhesion cell proliferation[41-43]. Interlocking block scaffolds provide a large surface area, facilitating cell proliferation and osteogenic differentiation of mesenchymal stem cells (MSCs)[44].

Dual growth factor delivery on bone regeneration significantly improves vascular growth and bone growth[45]. The combination of BMP-2 with BMP-7 was shown to enhance bone morphogenesis[46]. Therefore, developing a scaffold that could deliver a combination of BMP-2 with BMP-7 in a time-dependent manner would be a viable bone graft for bone healing. In the previous study, we found that a combination of BMP-2 and BMP-7 enhanced osteogenic differentiation, accelerated mineralization, shortened collagen formation time[44]. Based on observations in the previous study, we hypothesized that cells seeded scaffolds exhibit mechanics changes over time due to the maturation of ECM. To this end, we evaluated nanomechanical properties of the cells seeded scaffolds using Berkovich indenter tip and correlated mechanical properties changes with mRNA expression of bone-related genes, confocal and SEM imaging.

2. Materials and Methods

2.1 Modification of MMT clay

Na-MMT clay (SWy-2) was received from the Clay Minerals Society (Wyoming). The Na-MMT clay is modified with 5-aminovaleric acid described in detail in previous studies [47, 48]. In brief, preheated (60^{o}C) 5-aminovaleric acid solution was added to preheated (60^{o}C) MMT suspension and kept for stirring for one hour. After one hour, the obtained slurry was separated

using a centrifuge followed by drying at 70ºC, grinding, and sieving to obtain a fine powder. The 5-aminovaleric acid was purchased from Sigma-Aldrich.

2.2 Preparation of in situ HAPclay

The *in situ* HAP clay was prepared following the detailed steps described in previous studies[42, 49, 50]. Briefly, amino acid modified Na-MMT clay powder was poured into Na_2HPO_4 (J.T. Baker) solution and kept for stirring for 2 hours. Then, $CaCl_2$ (J.T. Baker) solution was added to the clay, Na_2HPO_4 suspension, and kept for stirring for 8 hours at pH 7.4. The precipitate obtained was separated using a centrifuge followed by drying at 70ºC, grinding, and sieving to obtain a fine powder.

2.3 Preparation of PCL/in situ HAPClay scaffolds

3D porous PCL/in situ HAPClay scaffolds were prepared following the steps described in detail in previous studies[40, 44]. In brief, the PCL (Sigma Aldrich) solution was prepared by dissolving 3.6 g (90%) of polymer in 40 ml of 1,4-dioxane (Sigma Aldrich). Another solution was prepared by dispersing 0.4 g (10%) of *in situ* HAPclay in 20 ml of 1,4-dioxane. The *in situ* HAPclay suspension was sonicated for 18 minutes for better dispersion of *in situ* HAPclay in dioxane. Sonicated *in situ* HAPclay solution was added to the polymer solution and kept for stirring for 2 hours. Then, the polymer HAPclay solution was poured into the 3D-printed molds. Designing and preparation of 3D printed mold described in the previous study[44]. Further, the freeze extraction method was used to obtain 3D scaffolds.

2.4 Preparation of scaffold sample for cell culture

PCL/ in situ HAPclay scaffolds were sterilized using a UV sterilization chamber for 45 minutes, followed by immersing in 100 % ethanol for 24 hours. Then the sterilized were washed in PBS to remove the ethanol from the scaffolds. BMP 2 (Genscript) and BMP 7 (Biovision) solutions were prepared by following the manufacturer's protocol at a concentration of 1µg/ml. Sterilized scaffolds were immersed into the freshly made 1:1 BMP-2 and BMP-7 solution for 24 hours. After 24 hours, BMP-2 and BMP-7 coated samples were kept in the cell culture media for 24 hours before using them for cell culture experiments. Initially, a combination of 5 X 10^4 osteoblast cells (hFOB) and 5 X 10^4 MSCs were seeded on each scaffold.

2.5 Cell lines and culture medium

The human osteoblast cell line (hFOB 1.19) was purchased from ATCC. The culture media consisted of 90% HyQ Dulbecco's Modified Eagle medium DMEM-12(1:1) from Hyclone, 10% fetal bovine serum (FBS) from ATCC, and 0.6% antibiotic solution (G418) from JR scientific. Human mesenchymal stem cells (MSCs) were purchased from Lonza and maintained in MSCGM™ Bulletkit™ medium. The Bulletkit™ medium was prepared by adding MSCGM™ SingleQuots™ (Lonza) to MSCBM™ (Lonza). We maintained cells at 37^{o}C and 5% CO_2 in a humidified incubator.

2.6 ELISA Assays

The amount of BMP-2 and BMP-7 released in the PBS were determined using the ELISA assay kits (BMP-2 Invitrogen kit, BMP-7 Invitrogen kit) following the manufacturers' instructions. We collected the supernatant at every 24hr interval followed by adding fresh PBS.

2.7 DNA quantification

Cell viability was performed by measuring DNA content according to the manufacturers' protocol (AccuBlue® Broad Range dsDNA Quantitation Kits). Briefly, the cell-seeded scaffolds were washed with PBS, and each scaffold was digested in 500 µl of cell lysis TE buffer. Then, scaffolds were kept at -80 °C followed by three freeze-thaw cycles at −80 °C and 37 °C. Further, the cells supernatants were collected after centrifugation. Finally, 10 µl of each diluted sample was mixed with 200 µl of working solution and incubated for 30 min at room temperature in the dark. The fluorescence was measured at 350 nm excitation/460 nm emission using a fluorescence microplate reader (BioTek).

2.8 Scanning electron microscopy

The tissue-cultured scaffold samples were washed with PBS and fixed with 2.5% glutaraldehyde followed by ethanol series treatment (10%, 30%, 50%, 70%, and 100% v/v) for dehydration. The samples were dried using hexamethyldisilazane after alcohol treatment. The samples were then carbon-coated and mounted on SEM stubs for observation using the JEOL JSM 6490LV scanning electron microscope.

2.9 Gene expression studies

Total RNA from the cell-seeded scaffolds was isolated and quantified using Direct-zol RNA MiniPrep kit (Zymo Research) and Nanodrop ND 2000 (Nanodrop products), respectively. Then, cDNA was prepared using 2 µg/µl of RNA, random primers, and M-MLV reverse transcriptase (Promega) in PCR thermal cycler (Applied Biosystems). Real-time polymerase chain reaction (PCR) experiment was performed using a 7500 Fast Real-Time PCR system (Applied Biosystems). Forward primer, reverse primer, SYBR Green dye, and cDNA were added to make a final volume of 20 µl and run using a thermal profile with a holding stage (2 min at 50 °C, 10 min

at 95 °C) and a cycling stage (40 cycles of 15 s at 95 °C, and 1 min at 60 °C). The mRNA expressions of Runt Related Transcription Factor 2 (RUNX2), Osteopontin (OPN), Osteocalcin (OCN), Bone sialoprotein (BSP), Alkaline phosphatase (ALP), LRP5, Wnt5a, and β-catenin were quantified and normalized to housekeeping gene glyceraldehyde-3-phosphate-dehydrogenase (GAPDH). For all the genes 2D 0 days sample were used as a control. Target gene expressions were analyzed using the comparative C_t method ($2^{-\Delta\Delta Ct}$). The sequence of primers used is shown in supplementary Table 1.

2.10 Analysis of nanomechanical response

Displacement controlled nanoindentation experiments on the hydrated scaffolds, cell-seeded scaffolds without BMPs coating, and cell-seeded scaffolds with BMPs coating in cell culture medium were performed using Berkovich diamond indenter fluid tip (three-sided pyramidal; 100-200 nm tip radius) using Hysitron Triboscope nanomechanical instrument (Minneapolis, MN) equipped with multimode AFM (nanoscope IIIa controller and J-type piezo scanner system) (Veeco Metrology, Santa Barbara, CA). Cell-seeded porous scaffolds were placed inside the custom-designed 3D printed holder and flushed with cell culture medium for the experiment. Subsequently, samples were placed onto the nanoindentation sample stage, and the whole tip-sample-fluid assembly was heated and maintained at 37ºC. For the entire duration of the experiments, extreme care was taken to ensure that the scaffolds were wholly immersed in the cell culture medium. Indentation experiments were performed at maximum indentation depths of 500, 1000, and 2000 nm, respectively, at loading and unloading rates of 25 nm/s.

The load-displacement curve of each test was carefully analyzed to separate scaffolds, cells, and mineralized ECM indentation responses. Contact stiffness was calculated by applying power-law fit to the initial unloading portion of the load-displacement curve and analytically differentiating

the power-law relation, following the Oliver-Pharr method [51]. Reduced modulus was calculated from the stiffness and contact area measurements using Hysitron analysis software. The elastic modulus for each indent was further determined from reduced modulus and is given by the following relation:

$$\frac{1}{E_r} = \frac{(1-\vartheta^2)}{E_s} + \frac{(1-\vartheta_i^2)}{E_i}$$

where, E_r=reduced elastic modulus; E_s=elastic modulus of sample; E_i=elastic modulus of indenter; ϑ_i= Poisson's ratio of indenter; ϑ_s= Poisson's ratio of the sample. In this work, we used the diamond indenter tip of elastic modulus 1141 GPa and Poisson's ratio of 0.07. Using Poisson's ratio of 0.5, as also commonly used in literature, we calculated elastic moduli of biological cells. In this work, all the experiments are performed under fully immersed conditions. For all the samples, at least 30 indents were made under each set of experimental conditions. We used triplicate samples in the experiments to ensure repeatability and reproducibility. In this work, at a particular depth, variation in elastic properties arises due to the presence of different constituents (porous scaffolds, cells, and mineralized ECM) possessing different physical/biological characteristics, thereby expected to exhibit their unique mechanical behavior. Under such a scenario, a range of modulus values was plotted to indicate the difference in elastic properties of cells, cell scaffolds, and Mineralized ECM.

2.11 Alizarin Red S Staining (ARS) and Quantification Assay

Cell-seeded scaffolds were fixed with 4% paraformaldehyde for 30 mins and washed with PBS three times (5 min each wash) to remove the residual fixative agent. Further, scaffolds were stained with Alizarin Red S dye (2 g/100 mL deionized water, pH = 4.10 to 4.15 and kept for 2 min 30 sec. After 2 min 30 sec, the scaffold was washed using cell culture grade water many times

to remove excess dye. Z-stacks of the samples were obtained using a Zeiss Axio Observer Z1 microscope equipped with an LSM700 laser-scanning module. Images were taken using a 639 nm laser light source. For image analysis, Imaris software was used. For quantification, stained samples were immersed into 700 µL of 10% acetic acid solution and incubated at room temperature for 5 min to solubilize the stain, and absorbance of the released Alizarin Red S stain was measured at 405 nm.

2.12 Statistical analysis

All the experiments were carried out in triplicates (n = 3) unless otherwise mentioned, and the data are presented as Mean value of triplicates ± standard derivation. The statistical significance (p-value) between the two groups is done using Student's unpaired *t-test. In contrast,* multiple comparisons are made using two-way ANOVA followed by an appropriate *post hoc* test (GraphPad Prism v8.4.2). Differences between the two groups were considered statistically significant when probability, $^{*}p < 0.05$.

3. Results and discussion

3.1 Release Kinetics of BMPs

The amount of BMP-2 and BMP-7 released from the scaffolds is measured by ELISA assay. Fig. 1A represents the percentage of cumulative content of released BMP-2 and BMP-7 over time from the scaffolds. We observed an initial burst of release in the first 24 h; about 40% of BMP-2 and BMP-7 releases occurred in the first 24 hr, followed by a slower release. According to literature, nonbonded interactions between components of the scaffold and BMPs govern the rate of BMPs release [52-54]. Since scaffold constituents are distributed homogeneously among samples, a slight

variation in the amount of BMP-2 or BMP-7 released from scaffolds was observed. However, because of difference in numbers of amino acids (BMP-2, 114 and BMP-7, 139) [55, 56] and functional groups in BMP-2 and BMP-7, a difference in release rate from the scaffolds was observed. Finally, after 15-day for BMP-7 and after 16-day for BMP-2, complete release was observed from the scaffolds.

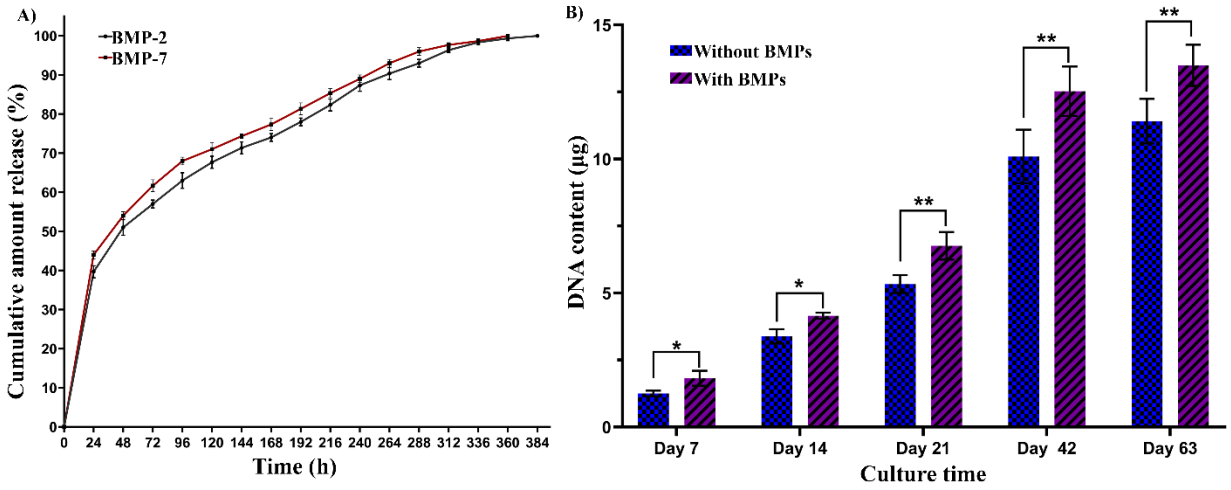

Fig. 1. Cumulative percentage release of BMP-2 and BMP-7 over time from the scaffolds in PBS (A), The proliferation of hMSCs and hFOB (DNA content) on BMPs coated and without BMPs scaffold samples at day-7, day-14, day-21, day-42, and day-63 (B). $*p < 0.05$, $**p < 0.01$, and $***p < 0.001$ indicate a significant difference between BMPs coated and without BMPs scaffold samples.

3.2 Coating with the BMPs enhanced the proliferation of hMSCs and hFOB

The hMSCs and hFOB were cultured on scaffolds for 63 days on both without BMPs and with BMPs coated nanoclay based porous scaffolds. The DNA quantification data showed a steady increase in DNA content in both culturing conditions over time. However, the amount of DNA was significantly higher in BMPs coated scaffolds than without BMPs scaffolds, as shown in Fig.

1B. In addition, the cell proliferation with BMPs coated samples showed an increase in DNA content, with some statistical significance ($*p < 0.05$) compared to day-7 without BMPs samples, indicating the effect of BMPs on hMSCs and hFOB proliferation. In contrast, at day-21 and later, BMPs coated samples exhibited a large increase in cell proliferation at statistically significant levels ($**p < 0.01$).

3.3 Cell Morphology

SEM micrographs of dry PCL/in situ HAPclay scaffold are shown in Fig. 2(A–C). The images indicate interconnecting porous microstructure. These scaffolds seem to have pore sizes in the range of less than 10 μm–300 μm. SEM micrographs of PCL/in situ HAPclay scaffold seeded with human MSCs and osteoblast cells for nine weeks are shown in Fig. 2(D–I). These images indicate attachment, spreading of cells on the scaffold, and formation of mineralized extracellular matrix (ECM) by the cells on these composite scaffolds. The red arrows indicate the mineralization on the scaffolds seeded with human MSCs and osteoblast cells. In addition, SEM micrographs show enhanced ECM formation on BMPs coated samples Fig. 2(G-I) compared with uncoated samples Fig. 2(D-F), indicating the effect of BMPs on mineralization.

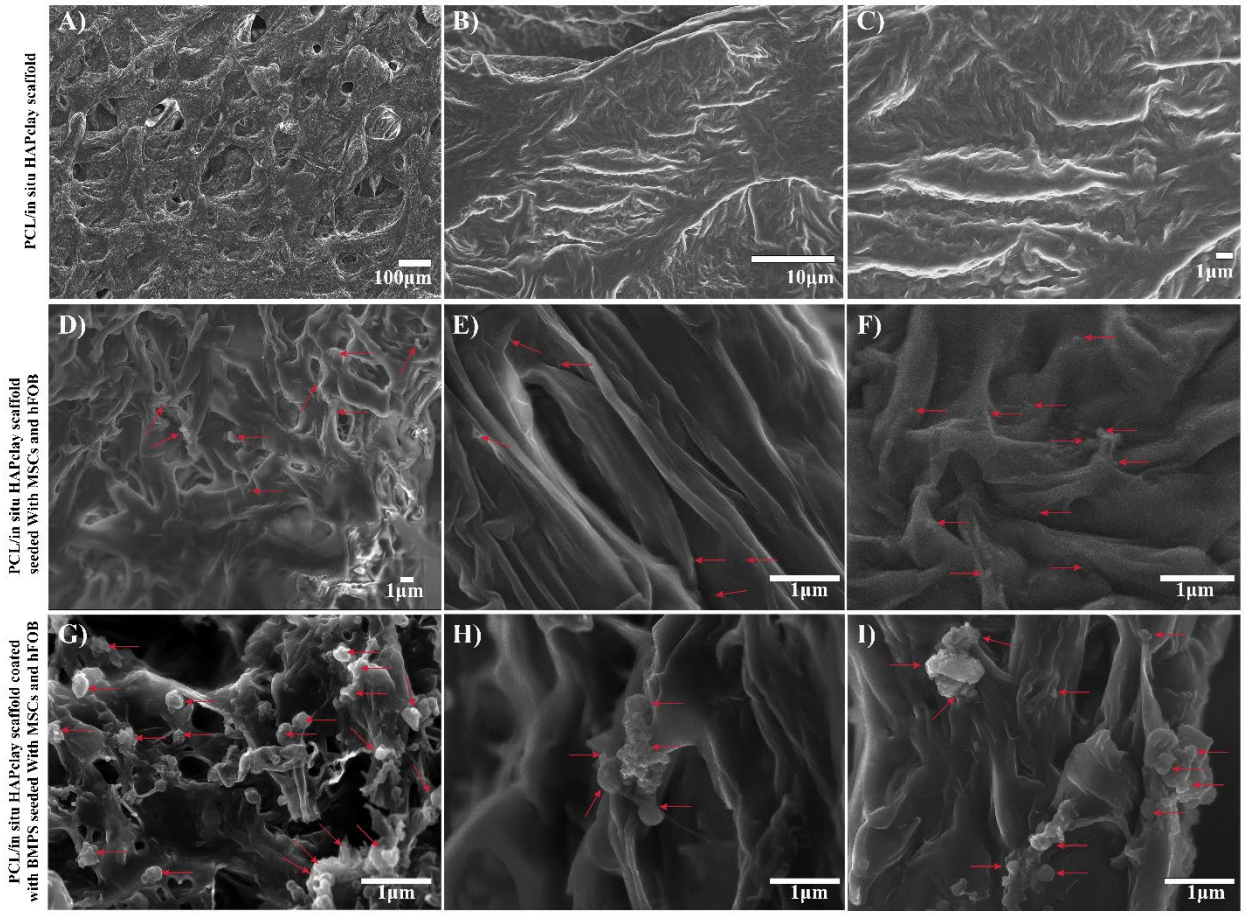

Fig. 2. SEM micrographs of PCL/ in situ HAPclay scaffolds (A-C) showing the interconnecting porous structure of the scaffold, SEM micrographs of hMSCs and hFOB cultured on bone-mimetic nanoclay scaffolds after 63 days indicating cell attachment, spreading, and mineralization on (D-F) without BMPs coated and (G-I) BMPs coated scaffold. As seen, attachment, spreading of cells on the scaffold, and formation of mineralized extracellular matrix (ECM) by the cells is observed on these composite scaffolds. The red arrows indicate the mineralization on the scaffolds seeded with human MSCs and osteoblast cells. Enhanced ECM formation is observed on BMPs coated samples (G-I) compared with uncoated samples D-F).

3.4 Osteogenic differentiation of hMSCs and hFOB and ECM formation on nanoclay-based scaffolds amplified by BMPs.

To evaluate the effect of BMPs on ECM formation on MSCs and hFOB cells seeded nanoclay-based scaffolds, we examined the expressions of ECM formation-related genes (OPN, OCN, and BSP). OPN, OCN, and BSP are bone markers, and the expression of these markers increases during osteoblast maturation and ECM formation. Fig. 3(A-C) represents the quantitative real-time PCR of OPN, OCN, and BSP expression, respectively. We found increased gene expression levels of ECM formation-related markers over time for both, without, and with BMPs coated scaffolds. However, a significant increase in ECM-related markers was observed with BMPs coated scaffolds. After 63-days almost ~2-fold increase in OPN level (A), ~2.5-fold increase in OCN level (B), and ~1.5-fold increase in BSP level (C) was observed in BMPs coated scaffolds compared with without BMPs coated scaffolds. They indicated the effect of BMPs on mineralization. To evaluate the effect of BMPs on osteogenic differentiation on MSCs and hFOB cells seeded nanoclay-based scaffolds, we examined the expressions of osteogenic differentiation-related genes (ALP and Runx2). Fig. 3(D, E) represents the quantitative real-time PCR of ALP and Runx2 expression, respectively. ALP is an osteogenic marker, indicating the early stage of osteoblastic differentiation, while Runx2 is a transcription factor that regulates osteoblastic differentiation. In the early stage of differentiation of MSCs, Runx2 has been shown to promote the differentiation of mesenchymal cells into osteoblasts; however, with the maturation of osteoblast, levels of Runx2 reduce. ALP expression has also been shown to downregulate during the maturation of osteoblasts and the formation of an extracellular matrix (ECM). We observed an increase in ALP and Runx2 expression at 7-days and 14-days, indicating osteogenic differentiation of MSCs for both samples. Later, at 21-days, 43-days, and 63-days, the expressions of ALP and

Runx2 were downregulated, indicating the maturation of osteoblast and ECM formation. With BMPs at 7-days, we observed a ~4-fold increase in Runx2 (D) and ALP (E) levels and ~3-fold increase at 14-days in Runx2 (D) and ALP (E) levels, compared with uncoated samples, indicating osteogenic differentiation of MSCs amplified by BMPs. BMPs play an important role on Runx2 level elevation through the Smad-dependent pathway. Then, an elevated level of Runx2 enhanced the osteogenic differentiation of MSCs and pre-osteoblast to mature osteoblast and enhanced bone formation[57]. With the maturation of osteoblast, the Runx2 level decreased[58]. Our results suggest the elevation of the Runx2 in the early stage is related to the osteogenic differentiation of MSCs and hFOB. Later, attenuation of the Runx2 level is associated with the maturation of the osteoblast and ECM formation. Fold increase in gene expression levels with BMPs coated samples is shown in Supplementary Table 2.

3.5 Osteogenesis in nanoclay-based scaffolds is mediated by the Wnt/β-catenin signaling pathway, enhanced by BMPs.

The Wnt/β-catenin signaling pathway plays a very important role in osteogenesis. To evaluate the effect of BMPs on the Wnt/β-catenin signaling pathway during osteogenesis on the nanoclay-based scaffolds, we analyzed the expressions of Wnt/β-catenin pathway-related genes (LRP5, Wnt5a, and β-catenin) in both scaffold systems. Fig. 3F describes the Wnt-5 expression level on with/without BMPs coated scaffolds over time. We observed a ~1.7-fold increase at day 7 and ~1.8-fold increase at day 14 in Wnt-5a expression level on BMPs coated samples compared with uncoated samples; then, for both samples, expression level decreases. Fig. 3G describes the LRP-5 expression level on with/without BMPs coated scaffolds over time. We found a ~1.5-fold increase at day 7 and ~1.8-fold increase at day 14 in LRP-5 expression level on BMPs coated

samples compared with uncoated samples; then, for both samples, expression level decreases. Fig. 3H describes the β-catenin expression level over time with/without BMPs coated scaffolds.

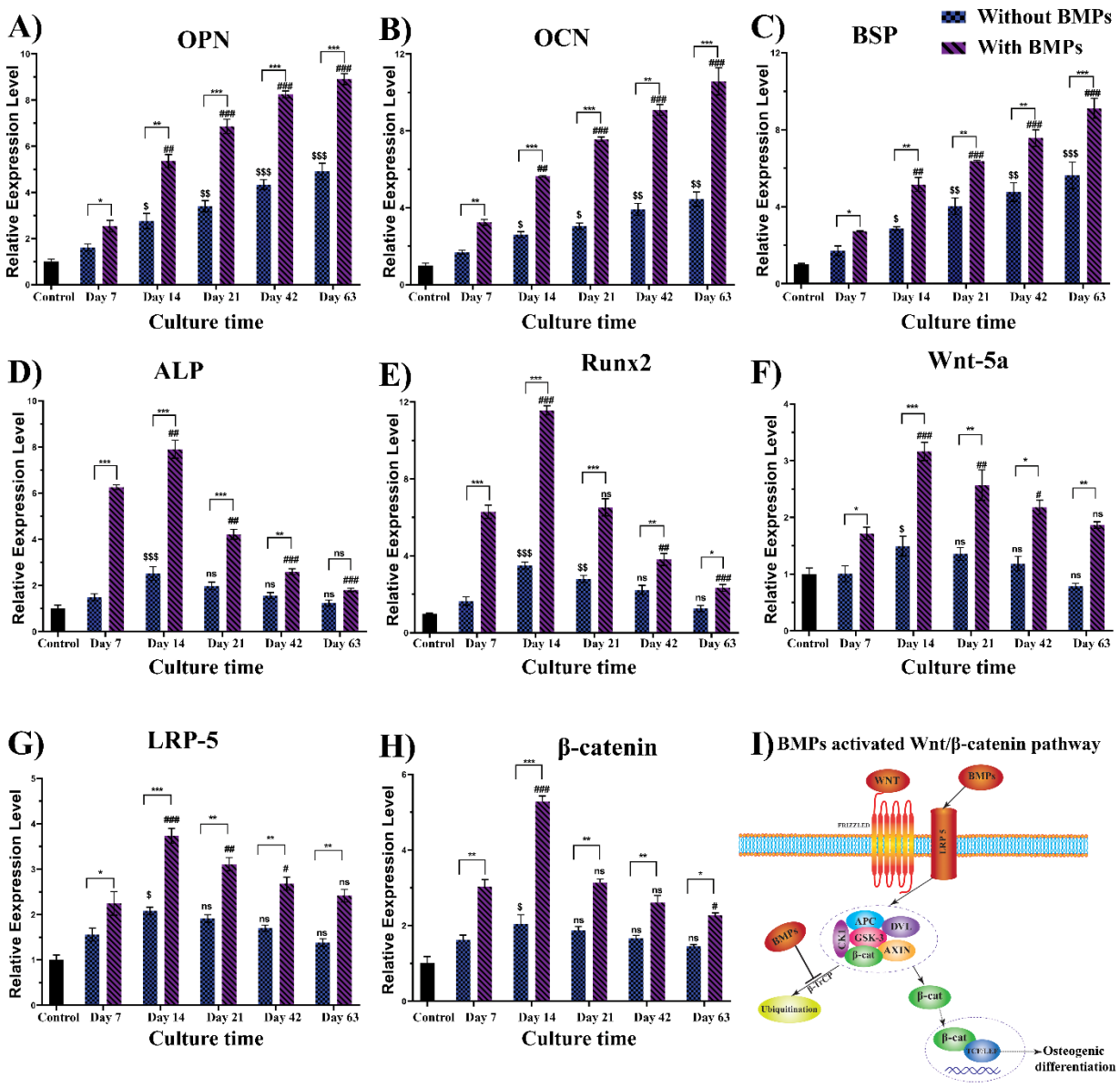

Fig. 3. Osteogenic differentiation of hMSCs and hFOB and ECM formation on nanoclay-based scaffolds enhanced by BMPs. Quantitative real-time PCR of gene expression for ECM formation-related markers A) OPN, B) OCN, and C) BSP. Quantitative real-time PCR of gene expression for osteogenic differentiation-related markers D) Runx2, and E) ALP. Osteogenesis in nanoclay-based

scaffolds is mediated by Wnt/β-catenin signaling pathway, enhanced by BMPs. F) Quantitative real-time PCR of gene expression for Wnt-related factors LRP-5, G) Quantitative real-time PCR of gene expression for Wnt-related factors Wnt-5a, and H) Quantitative real-time PCR of gene expression for Wnt-related factors β-catenin. Wnt-pathway I) illustrating how BMPs induced Wnt-pathway by inhibiting ubiquitination of β-catenin, and enhanced osteogenesis. *$p < 0.05$, **$p < 0.01$, ***$p < 0.001$ indicate a significant difference between BMPs coated scaffold and without BMPs coated scaffolds at 7-days, 14-days, 21-days, 42-days, and 63 days. $^{\$}p < 0.05$, $^{\$\$}p < 0.01$, $^{\$\$\$}p < 0.001$ indicate a significant difference between without BMPs 7-days with 14-days, 21-days, 42-days, and 63-days. $^{\#}p < 0.05$, $^{\#\#}p < 0.01$, $^{\#\#\#}p < 0.001$ indicate a significant difference between with BMPs 7-days with 14-days, 21-days, 42-days, and 63-days.

We observed a ~1.8-fold increase at day 7 and a ~2.5-fold increase at day 14 in β-catenin expression level on BMPs coated samples compared with uncoated samples for both samples, then, for both samples, expression level decreases. Fig. 3I describes the effect of BMPs on activation of the Wnt/β-catenin signaling pathway and upregulation of Wnt-related factors and ultimately enhance the osteogenic differentiation and bone formation. The activated Wnt/β-catenin pathway inhibits cytoplasmic degradation of β-catenin while promoting nuclear translocation of β-catenin, upregulating the bone-specific genes. β-catenin regulates the early stages of osteogenic differentiation and reduces bone maturation. We observed upregulated expressions of Wnt-related factors (LRP5, Wnt5a, β-catenin) at 7-days and 14-days while the expressions of all genes evaluated went down at 21-days and later on, indicating the maturation of bone. The number of fold increase in gene expression levels with BMPs coated sample compared with uncoated samples is shown in Supplementary Table 2.

3.6 Mineralized bone nodule formation is enhanced in the BMPs coated samples.

To assess the effect of BMPs on mineralization, we performed an Alizarin Red S assay. Scaffolds seeded with hMSCs and hFOB (without BMPs), scaffolds seeded with hMSCs, and hFOB coated with BMP-2 and BMP-7 (with BMPs) at one week, three weeks, six weeks, and nine weeks samples were stained with Alizarin Red S; the results are shown in Fig. 4A. Positive Alizarin Red S staining was observed for all the samples, indicating mineralized nodule formation. A significant difference in mineralization was observed between without BMPs and with BMPs samples. For all the samples, mineralized nodule formation increases over time. At nine weeks, maximum mineralized ECM formation was observed with BMPs coated samples, whereas the least amount of ECM formation was observed at one week with no BMPs coated samples. In Fig. 4A, the 3D view shows how ECM formation increases in each sample with time progression. A significant increase in ECM formation was observed from three weeks to six weeks and six weeks to nine weeks for both samples, which was further confirmed by quantification of the released ARS (Fig. 4B). Thus, the Alizarin Red S assay data indicates that BMPs enhance the mineralized bone nodule formation.

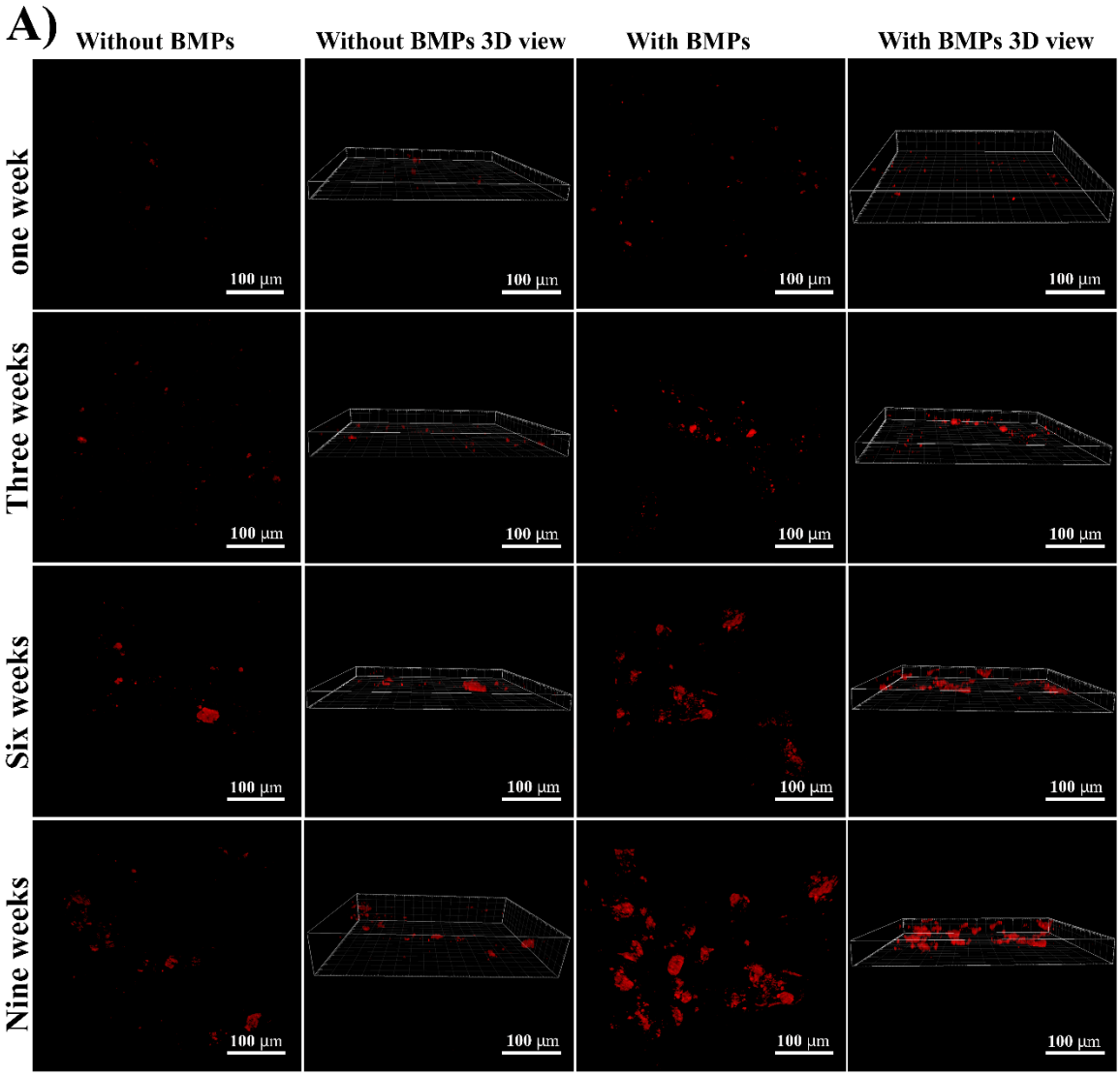
A)
Without BMPs
Without BMPs 3D view
With BMPs
With BMPs 3D view
one week
Three weeks
Six weeks
Nine weeks
100 µm

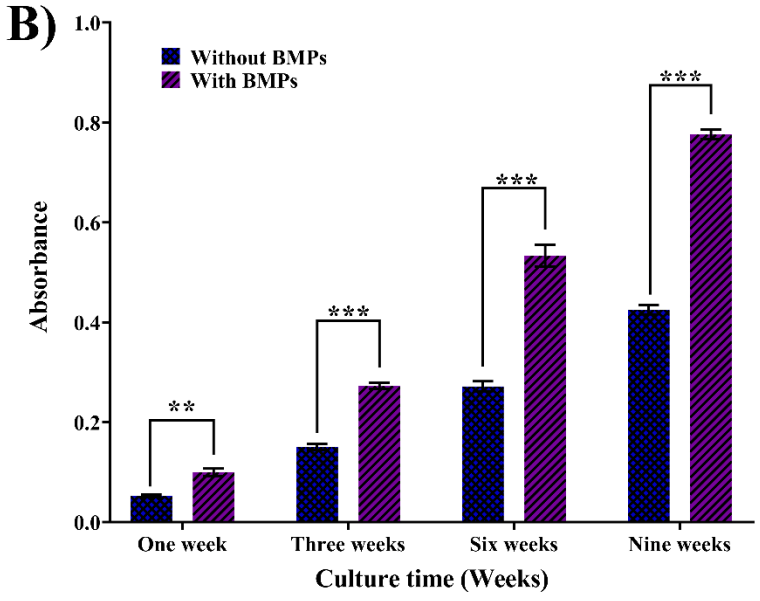
B)
Without BMPs
With BMPs
Absorbance
1.0
0.8
0.6
0.4
0.2
0.0
**
***
***
***
One week
Three weeks
Six weeks
Nine weeks
Culture time (Weeks)

Fig. 4. Confocal images and quantitative analysis to evaluate the effect of BMPs on mineralization. A) Confocal images with Alizarin Red S-stained scaffolds seeded with hMSCs and hFOB (without BMPs), scaffolds seeded with hMSCs, and hFOB coated with BMP-2 and BMP-7 (with BMPs) at one week, three weeks, six weeks, and nine weeks. 3D view showing the amount of mineralized ECM formation on each scaffold. Bar = 100 μm. As seen, ECM formation increases in each sample with time progression B) Graph shows quantification of ECM from the images showing more ECM formation with BMPs scaffolds. *$p < 0.05$, **$p < 0.01$, ***$p < 0.001$ indicate a significant difference between BMPs coated scaffold and without BMPs coated scaffolds at one week, three weeks, six weeks, and nine weeks.

3.7 Mechanical properties of the scaffolds decrease with the hydration period progression.

First, we investigated the mechanical properties of scaffolds in a hydrated state using instrumented indentation, focusing on the effect of hydration time on elastic modulus and indentation hardness. Here the depth-controlled nanoindentation tests were performed on scaffolds that had been hydrated for various periods, with indentation depths of 500 nm, 1000 nm, and 2000 nm. Fig. 5 (B-D) represents the load-displacement indentation curves for hydrated scaffolds at various indentation depths. In contrast, Fig. 5 (E-G) display Young's modulus and indentation hardness for the hydrated scaffold as a function of imposed indentation depth and hydration period.

It can be seen from Fig. 5. (B-D) that the maximum indentation loads for scaffold hydrated for a similar period increases with the increasing indentation depth. However, the maximum indentation load for equivalent indentation depths decreases as the scaffold hydrates. In general, wet environments alter the mechanical characteristics of polymers, owing to the plasticizing effect of water[59]. Earlier studies from our group have shown that organomodified nanoclay particles

alter the crystallinity of polymer nanocomposites. Adding HAP nanoparticles to PCL composite scaffolds changes the degradation rate [60-62]. It has also been observed that the incorporation of calcium phosphate-based nanoparticles also impacts polymer chain configuration [62]. The gradual decrease in the PCL/in situ HAPclay scaffold's mechanical properties observed here, therefore, can be attributed to its degradation in an aqueous environment from one week to nine weeks of hydration.

The elastic modulus and indentation hardness corresponding to each indentation represented the local behavior of the scaffold around the indented site. The interspersed lamellar structure with interconnected porosities is an intrinsic feature of PCL composite scaffolds containing in situ HAPclay[40]. Therefore, the range of elastic modulus and indentation hardness of the scaffolds in the hydrated condition obtained here fluctuated moderately. It has also been observed that the scaffolds' elastic modulus and indentation hardness decreases as the depth of the applied indentation increases. The material behavior observed here could be due to the indentation size effect (ISE) induced by intrinsic structural characteristics of materials, which causes hardness and elastic modulus to decrease as indentation depth increases. Several reasons for ISE have been proposed in recent decades, including the well-known strain gradient plasticity hypothesis[63], contact surface variation[64], dislocation nucleation[65], and microfracture mechanisms [66]. However, in this case, the SEM images (Fig. 2(A-C)) for the scaffold demonstrate that the porous scaffold structure contains small nano-pores and macroscopic defects such as big macro-pores. Therefore, when the penetrating indenter travels a greater depth in the scaffold, it is more likely to encounter a large sub-surface macro-pore or voids, causing a more rise in depth of penetration at a lower indentation load and thus affecting a larger area of contact, resulting in a lower modulus

value. In contrast, the low penetration depth resulted in a smaller contact area; therefore, the modulus calculated would be on the higher side, as shown in our results.

At the 500 nm penetration depth, the indenter captures the indentation response of a relatively small layer of scaffold surface; therefore, it appears that it is capturing the mechanical properties of the mixture of scaffold constituents. As a result, the elastic modulus value achieved here by 500 nm indentation depth is larger than the elastic modulus values acquired here by 1000 nm and 2000 nm indentation depth. However, indentation depths of 1000 nm and 2000 nm penetrate deeper into the scaffold and capture the impacts of the porosity on the mechanical properties of the scaffold, resulting in capturing the bulk properties of the scaffold system. In addition, all the unloading curves demonstrate considerable hysteresis compared to the loading curves in load-displacement plots, demonstrating that large plastic deformation occurs during the nanoindentation process.

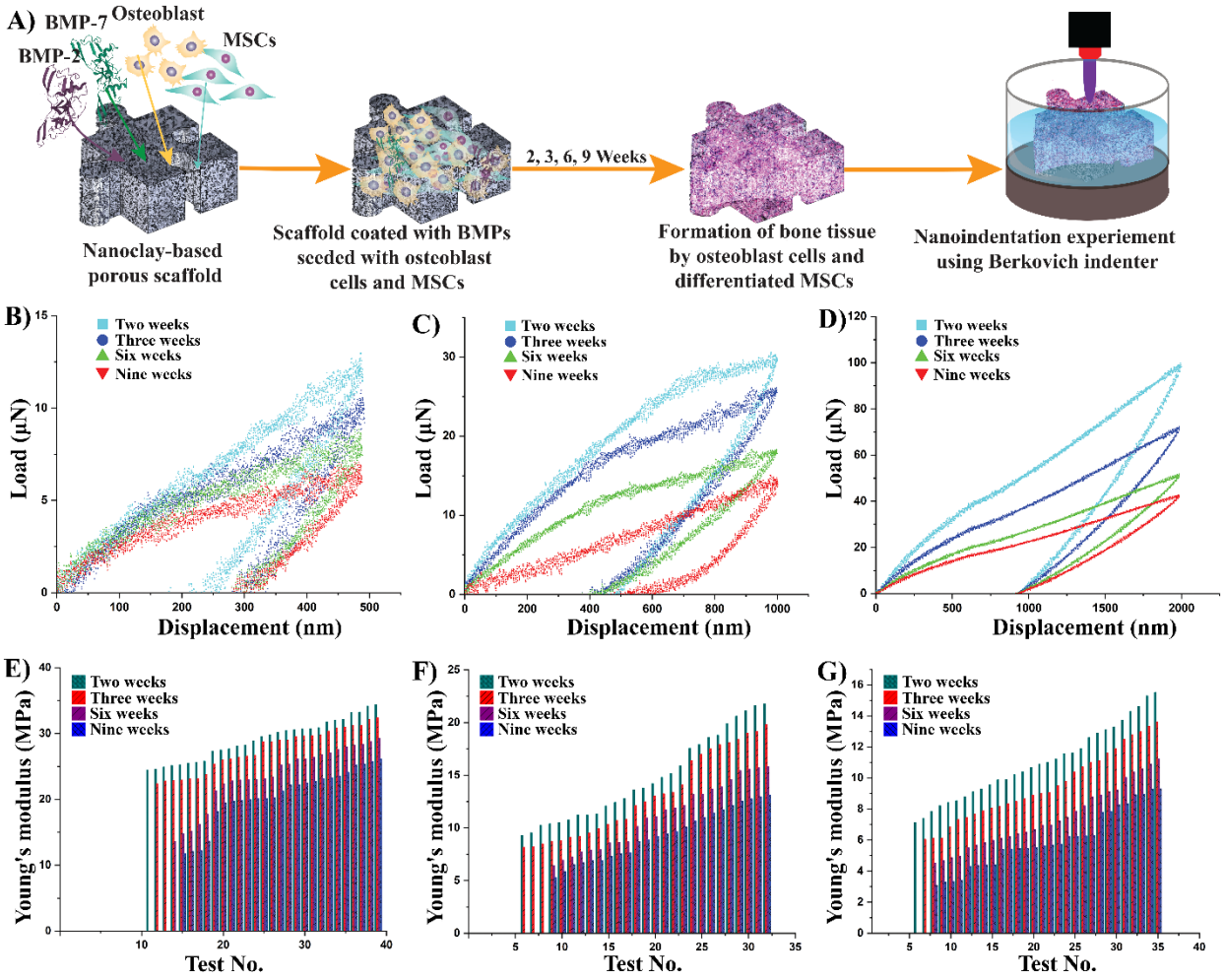

Fig 5. A) Schematic showing steps of coating with BMP-2/BMP-7, co-culture hMSCs/hFOB followed by the workflow of nanoindentation experiment. Initially, BMP-2/-7 coated scaffolds are seeded with hMSCs and hFOB. Further, the change in nanomechanical properties of the cells seeded scaffolds was determined using a Berkovich diamond indenter fluid tip using Hysitron Triboscope nanomechanical instrument. Typical nanoindentation load–depth curves of hydrated scaffolds at 500 nm (B), 1000 nm (C), and 2000 nm (D) indentation depths. (E), (F) and (G) represent the elastic modulus (E) as a function of indentation depth of 500 nm, 1000 nm, and 2000 nm, respectively.

3.8 Mechanical properties of the cells seeded scaffolds increase over time.

Fig. 6 (A-F) shows a typical load-displacement indentation graph for scaffolds seeded with hMSCs and hFOB without BMPs. The elastic modulus values derived from load-displacement plots for indentation depths of 500 nm, 1000 nm, and 2000 nm are shown in Fig. 6 (G) (H) and (I), respectively. As illustrated in Fig. 6(A-F) for scaffolds seeded with hMSCs and hFOB, the maximum indentation load and elastic modulus at 500 nm, 1000 nm, and 2000 nm indentation depth increase over time as the cells in the scaffolds start forming ECM and maturation of ECM occurred from one week to nine weeks. However, as the indentation depths increase, the elastic modulus decreases for the scaffolds cell-seeded for an equal period of time.

The data points in Fig. 6 (G) (H) and (I) show that the elastic modulus of the scaffold varied substantially across all indentation depths. Considering that each scaffold constituent is distributed randomly throughout the whole scaffold volume, the lower values of elastic modulus mainly indicate the region of the clay matrix with a low proportion of hard inclusions. Conversely, higher elastic modulus values mainly indicate the region of the clay matrix with a large proportion of small hard inclusions.

Because most biological samples, particularly biological cells and tissues, are neither ideal solids nor ideal liquids, they display both elastic and viscous responses and are hence referred to as viscoelastic[67]. Based on the wide range of elastic moduli values obtained for all indentation depths, three distinct zones of indentation response may be identified: soft, semi-hard, and hard. The elastic modulus in the range of 2.5 MPa to 7 MPa represents the microscopic mechanical behavior of bone cells on a scaffold (porous matrix) tested for all indentation depths. The soft region demonstrated here shows a soft cellular material like deformation response, consistent with the previously described cell indentation results[68]. Furthermore, the intermediate range of elastic modulus (15 to 50 MPa for 500 nm and 1000 indentation depth, and 12 to 18 MPa for 2000

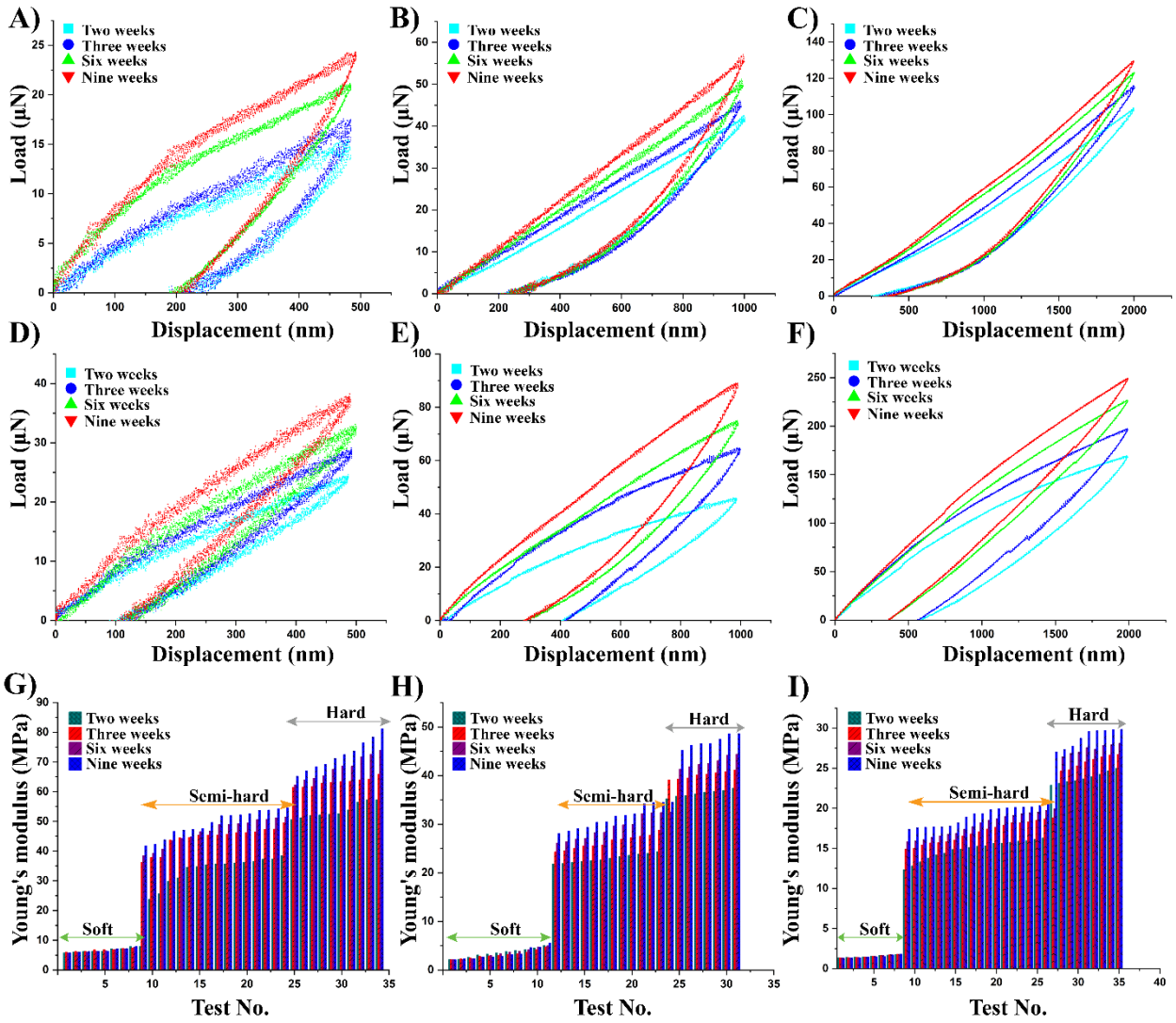

Fig 6. Nanoindentation load-displacement curves, elastic modulus (E) of scaffolds seeded with hMSCs and hFOB. Representative nanoindentation load-displacement curves from semi-hard areas of cells seeded scaffolds at indentation depths of 500 nm, 1000 nm, and 2000 nm are shown in (A), (C), and (C), respectively. The representative nanoindentation load-displacement curves from the hard regime of cells seeded scaffolds at indentation depths of 500 nm, 1000 nm, and 2000 nm are shown in (D), (E), and (F), respectively. The elastic modulus values at 500 nm, 1000 nm, and 2000 nm indentation depths are shown in (G), (H), and (I), respectively.

indentation depth) represents a mechanical characteristic of a mixed zone made up of cell scaffold matrix and small-sized hard mineral inclusions (semi-hard region). The elastic moduli values in the semi-hard region represent the transition region between the soft cellular matrix and stiff mineral matrix. Finally, the higher range of elastic moduli (35 to 85 MPa for 500 nm and 1000 indentation depth, and 22 to 35 MPa for 2000 indentation depth) represents a scaffold matrix zone that exhibits stiff deformation behavior of large-sized rigid minerals inclusions. Considering the mineral formation over time (shown in Fig. 4) in conjunction with the elastic modulus values presented in Fig. 6, we can conclude that small rigid mineral inclusion in the scaffold matrix at the microscopic scale can substantially influence the overall bulk mechanical characteristics of the scaffold system.

The elastic modulus values obtained from nanoindentation of BMP coated scaffold shows a trend similar to that of BMP uncoated scaffold, where maximum indentation load and elastic modulus for all indentation depths increased over time as the cells in the scaffolds began to form ECM and maturation of ECM occurred from one week to nine weeks. Fig. 7 (A–F) represents typical load-displacement graphs for nanoindentation on scaffolds seeded with hMSCs and hFOB with BMPs. Fig. 7 (G) (H) and (I) show the elastic modulus values derived from load-displacement plots of nanoindentation tests for indentation depths of 500 nm, 1000 nm, and 2000 nm, respectively. Fig. 7 (A-F) shows that for scaffolds seeded with hMSCs and hFOB with BMPs, the peak indentation load and elastic modulus for all indentation depth (500 nm, 1000 nm, and 2000 nm) increase with time as the cells in the scaffolds continues to generate ECM over time.

Here, similar to scaffolds seeded without BMPs, a wide range of elastic modulus of the scaffold is observed (for all indentation depths), indicating three different indentation response zones: soft, semi-hard, and hard. The soft material zone identified here has an elastic modulus

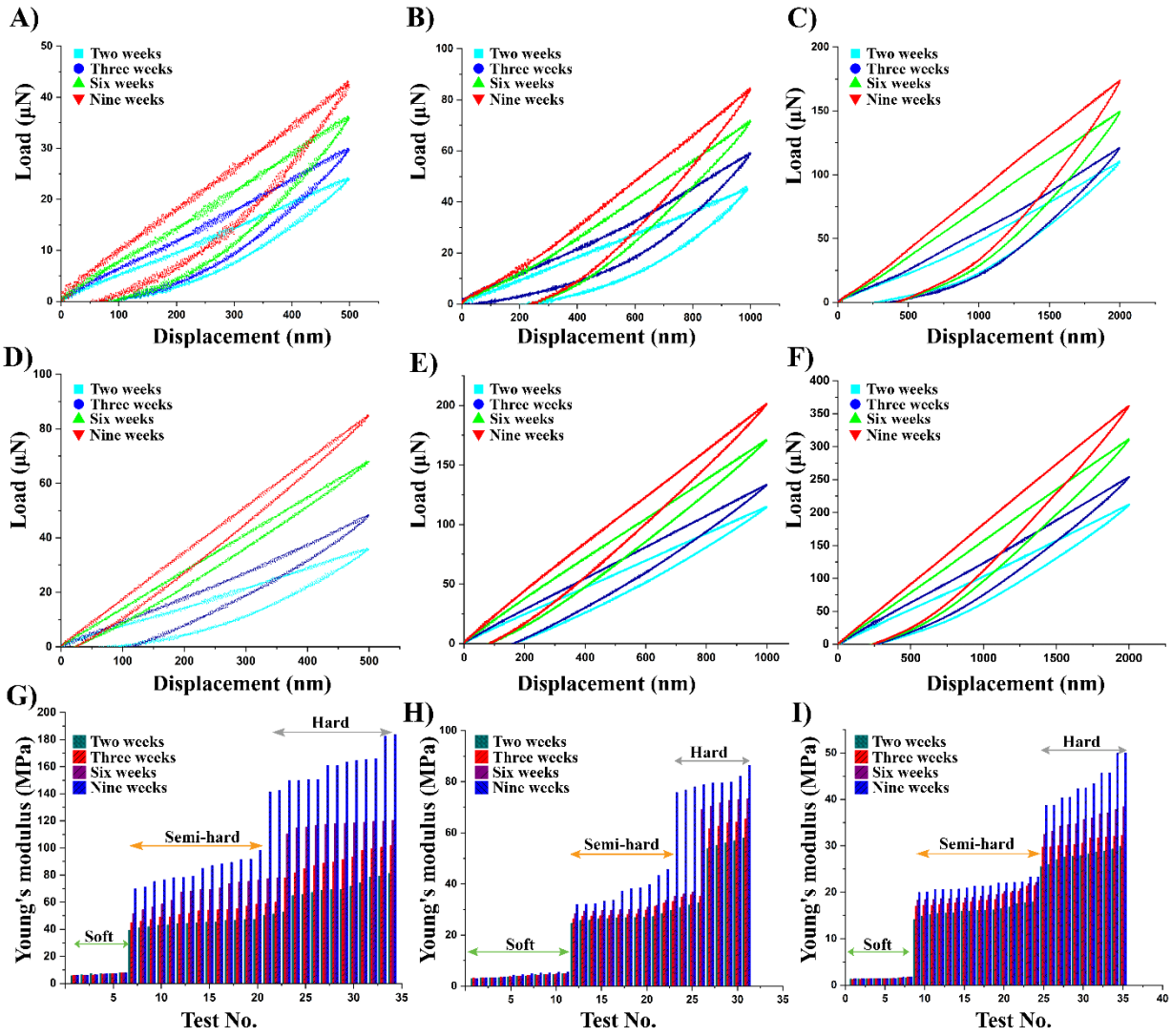

Fig. 7. Nanoindentation load-displacement curves, elastic modulus (E) of scaffolds seeded with hMSCs and hFOB coated with BMP-2 and BMP-7. Representative nanoindentation load-displacement curves from semi-hard areas of cell-seeded scaffolds at indentation depths of 500 nm, 1000 nm, and 2000 nm are shown in (A), (B), and (C), respectively. Representative nanoindentation load-displacement curves from the hard regime of cells seeded scaffolds are shown in (D), (E), and (F) for the indentation depths of 500 nm, 1000 nm, and 2000 nm, respectively. The elastic modulus values at 500 nm, 1000 nm, and 2000 nm indentation depths are shown in (G), (H), and (I), respectively.

ranging from 3 MPa to 7.5 MPa, representing the microscopic mechanical behavior of bone cells on a porous scaffold matrix. Furthermore, the intermediate elastic modulus range (35 to 100 MPa for 500 nm and 1000 indentation depth, and 18 to 28 MPa for 2000 indentation depth) constitutes a mechanically distinctive semi-hard zone. Lastly, in the hard regime, the range of elastic modulus (85 to 190 MPa for 500 nm and 1000 indentation depth, and 40 to 55 MPa for 2000 indentation depth) observed characterizes the scaffold matrix made up of very stiff minerals inclusions. The semi-hard and hard regions report a nearly two-fold increase in the elastic modulus in scaffold coated with BMPs compared with scaffold uncoated with BMPs at nine weeks. Fig. 8 (A-C) summarizes the young's modulus values determined from nanoindentation tests performed on hydrated scaffolds, cell-seeded scaffolds without BMPs, and cell-seeded scaffolds with BMPs at indentation depths of 500 nm, 1000 nm, and 2000 nm. A 67.4%, 24.5% and 12.3% increase in elastic modulus of semi-hard regions is observed with the addition of BMPs at 500 nm, 1000 nm and 2000 nm indentation (Supplementary Table 3). A 120.4%, 69.2% and 54.2% increase in elastic modulus of hard regions is observed with the addition of BMPs at 500 nm, 1000 nm and 2000 nm indentation (Supplementary Table 3). The values presented here are an average of over 100 nanoindentation test data points for each indentation depth, with standard deviations indicating the range of values where the elastic modulus converges. To begin, in the case of hydrated scaffolds, the elastic modulus values consistently decreased with increasing hydration period for all indentation depths. Thus, the results presented here greatly accord with our previous studies on the degradation of the scaffold in aquatic environments[60], where the degradation of the scaffold and reduction of mechanical integrity is suggested to result in substantially reduced compressive strength and modulus over time. As shown in Fig. 8, For the cell-seeded scaffold with and without BMPs, the elastic modulus values increased with time (from one week to nine weeks) for all

indentation depths. However, the cell-seeded scaffold with BMPs showed significantly higher elastic modulus and improved mechanical strength than those without BMPs over time. A 120% increase in elastic modulus at 500 nm indentation on scaffolds coated with BMPs indicates more ECM formation, significantly enhancing the overall mechanical characteristics of scaffolds over time, making them more suitable for possible uses in critical bone defect treatment. In addition, for a given indentation depth, peak loads increase over time for both BMP coated and uncoated scaffolds. The peak loads for hard regions in BMP coated scaffolds are significantly higher (~201 μN) as compared to uncoated scaffolds (~89 μN) at 1000 nm after 9 weeks. Significant increases are also observed in other regions. Simultaneously, elastic modulus at 9 weeks increases for BMP coated scaffolds from ~47 MPa to 80 MPa for hard regions at 1000nm (Supplementary Table 4).

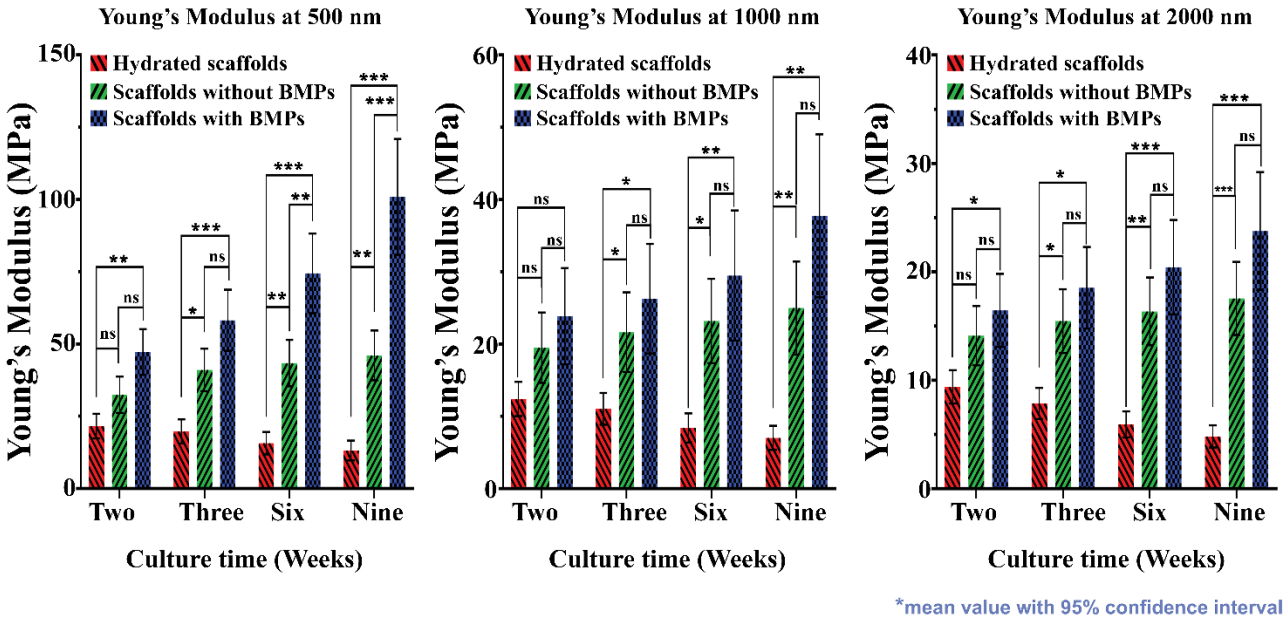

Fig. 8. Elastic modulus (E) of the hydrated scaffold, scaffolds seeded with hMSCs and hFOB, scaffolds seeded with hMSCs and hFOB coated with BMP-2 and BMP-7 at two weeks, three weeks, six weeks, and nine weeks (A), (B), and (C) at indentation depths of 500 nm, 1000 nm, and

2000 nm, respectively. $*p < 0.05$, $**p < 0.01$, and $***p < 0.001$ indicate a significant difference between BMPs coated and without BMPs scaffold samples.

This is consistent with increased mineralized nodule formations and ECM formations shown in Fig. 4. These in turn result from enhanced osteogenic differentiation of osteoblasts mediated by the Wnt/β-catenin signaling pathway, enhanced by BMPs. Thus, the cascade of events initiated by the BMPs impacts bone growth at time intervals much longer than the BMP presence in the scaffolds.

In our previous work, we observed that, with the co-culture of osteoblast and MSCs cells and combination of BMP-2, BMP-7 with a unique interlocking scaffolds, initiation of ECM formation started as early as three days, where with the control, without BMP-2 and 7 sample, ECM formation was not observed before day 11[21]. In this study, samples without BMP-2 and 7 were kept as a control. As shown in the figure 2, 3, 4, 6, 7, enhanced ECM formation was observed with cells seeded scaffolds with BMPs compared with cells seeded scaffolds without BMPs. In the figure 4, quantification of ECM showing the amount of ECM formed with uncoated scaffolds at nine weeks is less than the ECM formed with BMPs samples at six weeks. Results demonstrate that with the combination of BMPs, accelerated bone healing was observed as compared with uncoated scaffolds.

4. Conclusion

In this study, we report changes to nanomechanical properties of scaffolds over a period of nine weeks during osteogenesis with the influence of BMPs on nanoclay interlocking scaffolds. The changes in the elastic modulus of the scaffolds are measured with the formation of ECM over time. The mechanical properties observed at different indentation depths (500 nm-2000 nm) are measured using displacement controlled nanoindentation. Furthermore, the indentation results

showed that scaffolds degrade in culture media and the elastic modulus reduces over time. In contrast, in cells seeded scaffolds, the cells form ECM, and elastic modulus increases over time. In addition, BMP-2/BMP-7 coated scaffolds showed higher elastic modulus values (with as much as 120% increase) indicating enhanced ECM formation in BMPs coated samples. BMPs enhanced cell proliferation is observed in the nanoclay based scaffold. Gene expression studies indicate a significant increase in the bone related protein and osteogenesis with BMPs coated samples compared to without BMPs samples, indicating that BMPs play an essential role in osteogenesis and ECM formation. In addition, alizarin Red S staining images show a significant increase in the mineralized bone nodules with BMPs coated samples compared with without BMPs samples suggesting that BMPs play a crucial role in mineralized ECM formation. The BMP release experiments indicate that 100% release occurs at about 2.3 weeks. Interestingly, the data obtained on mechanical properties as well as gene expressions indicate substantial increase at well past the 2.3-week period.

In summary, we report changes in the nanomechanical properties during osteogenesis and bone tissue formation in BMP coated porous scaffolds over extended time periods up to nine weeks. Furthermore, the results indicate that the formation of ECM enhances the elastic modulus of the scaffolds. The role of BMPs in ECM formation lasts much longer (at nine weeks) than the release rate in the scaffolds (100% at 2.3 weeks). Thus, BMPs play a crucial role on initial stages of osteogenesis in the scaffolds. This study provides valuable insight into the mechanisms of the BMPs associated with bone tissue formation through the activation of the Wnt/β-catenin signaling pathway and upregulation of Wnt-related factors. Thus, an initial burst of BMPs can influence long term bone formation without the need for continuous BMP release. Hence this study has potential therapeutic applications for bone regeneration.

Declaration of Competing Interest

The authors declare no conflict of interest.

Acknowledgements

This work is made possible through the support of ND Department of Commerce grant 19-11-G-237. Partial support from NSF OIA NDACES-1946202 and NIH/UND (DaCCoTA) NIH-U54GM128729 is also acknowledged. Author K Kundu would also like to acknowledge support from the NDSU Center for Engineered Cancer Testbeds. Authors would also like to acknowledge Dr. Tao Wang, Manager, core biology facility at NDSU, for help with qRT PCR and Dr. Pawel Borowicz, Advanced Imaging and Microscopy (AIM) Core Lab, for confocal imaging.

Author Contributions

K. S. Katti (Conceptualization; Data curation; Formal analysis; Funding acquisition; Investigation; Methodology; Project administration; Resources; Supervision; Roles/Writing - review & editing), D. R. Katti (Conceptualization; Data curation; Formal analysis; Funding acquisition; Investigation; Methodology; Project administration; Resources; Software; Supervision; Roles/ Writing - review & editing), K. Kundu (Data curation; Formal analysis; Investigation; Methodology; Roles/Writing - original draft), S. Jaswandkar (Data curation; Formal analysis; Investigation; Methodology; Roles/Writing - original draft)

References

[1] D.J. Prolo, J.J. Rodrigo, Contemporary bone graft physiology and surgery, Clinical Orthopaedics and Related Research® 200 (1985) 322-342.

[2] A.S. Brydone, D. Meek, S. Maclaine, Bone grafting, orthopaedic biomaterials, and the clinical need for bone engineering, Proceedings of the Institution of Mechanical Engineers, Part H: Journal of Engineering in Medicine 224(12) (2010) 1329-1343.
[3] A.-M. Wu, C. Bisignano, S.L. James, G.G. Abady, A. Abedi, E. Abu-Gharbieh, R.K. Alhassan, V. Alipour, J. Arabloo, M. Asaad, Global, regional, and national burden of bone fractures in 204 countries and territories, 1990–2019: a systematic analysis from the Global Burden of Disease Study 2019, The Lancet Healthy Longevity 2(9) (2021) e580-e592.
[4] J.O. Hollinger, J.C. Kleinschmidt, The critical size defect as an experimental model to test bone repair materials, The Journal of craniofacial surgery 1(1) (1990) 60-68.
[5] K. Quan, Q. Xu, M. Zhu, X. Liu, M. Dai, Analysis of risk factors for non-union after surgery for limb fractures: a case-control study of 669 subjects, Frontiers in Surgery 8 (2021).
[6] D.J. Hak, D. Fitzpatrick, J.A. Bishop, J.L. Marsh, S. Tilp, R. Schnettler, H. Simpson, V. Alt, Delayed union and nonunions: epidemiology, clinical issues, and financial aspects, Injury 45 (2014) S3-S7.
[7] T.A. McCall, D.S. Brokaw, B.A. Jelen, D.K. Scheid, A.V. Scharfenberger, D.C. Maar, J.M. Green, M.R. Shipps, M.B. Stone, D. Musapatika, Treatment of large segmental bone defects with reamer-irrigator-aspirator bone graft: technique and case series, Orthopedic Clinics 41(1) (2010) 63-73.
[8] B.M. Desai, Osteobiologics, American journal of orthopedics (Belle Mead, NJ) 36(4 Suppl) (2007) 8-11.
[9] S.M. Quinnan, C. Lawrie, Optimizing bone defect reconstruction—balanced cable transport with circular external fixation, Journal of orthopaedic trauma 31(10) (2017) e347-e355.
[10] N.T. Bennett, G.S. Schultz, Growth factors and wound healing: biochemical properties of growth factors and their receptors, The American Journal of Surgery 165(6) (1993) 728-737.
[11] D.J. Baylink, R.D. Finkelman, S. Mohan, Growth factors to stimulate bone formation, Journal of Bone and Mineral Research 8(S2) (1993) S565-S572.
[12] M. Raida, A.C. Heymann, C. Günther, D. Niederwieser, Role of bone morphogenetic protein 2 in the crosstalk between endothelial progenitor cells and mesenchymal stem cells, International journal of molecular medicine 18(4) (2006) 735-739.
[13] M.R. Urist, Bone: Formation by Autoinduction, Science 150(3698) (1965) 893.
[14] D.O. Wagner, C. Sieber, R. Bhushan, J.H. Borgermann, D. Graf, P. Knaus, BMPs: From Bone to Body Morphogenetic Proteins, Science Signaling 3(107) (2010) 6.
[15] T. Katagiri, N. Takahashi, Regulatory mechanisms of osteoblast and osteoclast differentiation, Oral Diseases 8(3) (2002) 147-159.
[16] C. Thouverey, J. Caverzasio, Focus on the p38 MAPK signaling pathway in bone development and maintenance, Bonekey Reports 4 (2015) 8.
[17] A. Oryan, S. Alidadi, A. Moshiri, A. Bigham-Sadegh, Bone morphogenetic proteins: A powerful osteoinductive compound with non-negligible side effects and limitations, Biofactors 40(5) (2014) 459-481.
[18] D.S. Keskin, A. Tezcaner, P. Korkusuz, F. Korkusuz, V. Hasirci, Collagen-chondroitin sulfate-based PLLA-SAIB-coated rhBMP-2 delivery system for bone repair, Biomaterials 26(18) (2005) 4023-4034.
[19] J.N. Zara, R.K. Siu, X.L. Zhang, J. Shen, R. Ngo, M. Lee, W.M. Li, M. Chiang, J. Chung, J. Kwak, B.M. Wu, K. Ting, C. Soo, High Doses of Bone Morphogenetic Protein 2 Induce Structurally Abnormal Bone and Inflammation In Vivo, Tissue Engineering Part A 17(9-10) (2011) 1389-1399.
[20] H.S. Yang, W.G. La, S.H. Bhang, T.J. Lee, M. Lee, B.S. Kim, Apatite-Coated Collagen Scaffold for Bone Morphogenetic Protein-2 Delivery, Tissue Engineering Part A 17(17-18) (2011) 2153-2164.
[21] S. Govender, C. Csimma, H.K. Genant, A. Valentin-Opran, Y. Amit, R. Arbel, H. Aro, D. Atar, M. Bishay, M.G. Borner, P. Chiron, P. Choong, J. Cinats, B. Courtenay, R. Feibel, B. Geulette, C. Gravel, N. Haas, M. Raschke, E. Hammacher, D. van der Velde, P. Hardy, M. Holt, C. Josten, R.L. Ketterl, B. Lindeque, G. Lob, H. Mathevon, G. McCoy, D. Marsh, R. Miller, E. Munting, S. Oevre, L. Nordsletten, A.

Patel, A. Pohl, W. Rennie, P. Reynders, P.M. Rommens, J. Rondia, W.C. Rossouw, P.J. Daneel, S. Ruff, A. Ruter, S. Santavirta, T.A. Schildhauer, C. Gekle, R. Schnettler, D. Segal, H. Seiler, R.B. Snowdowne, J. Stapert, G. Taglang, R. Verdonk, L. Vogels, A. Weckbach, A. Wentzensen, T. Wisniewski, B.S. Grp, Recombinant human bone morphogenetic protein-2 for treatment of open tibial fractures - A prospective, controlled, randomized study of four hundred and fifty patients, Journal of Bone and Joint Surgery-American Volume 84A(12) (2002) 2123-2134.
[22] G.M. Calori, L. Tagliabue, L. Gala, M. d'Imporzano, G. Peretti, W. Albisetti, Application of rhBMP-7 and platelet-rich plasma in the treatment of long bone non-unions A prospective randomised clinical study on 120 patients, Injury-International Journal of the Care of the Injured 39(12) (2008) 1391-1402.
[23] G.E. Friedlaender, C.R. Perry, J.D. Cole, S.D. Cook, G. Cierny, G.F. Muschler, G.A. Zych, J.H. Calhoun, A.J. LaForte, S. Yin, Osteogenic protein-1 (bone morphogenetic protein-7) in the treatment of tibial nonunions - A prospective, randomized clinical trial comparing rhOP-1 with fresh bone autograft, Journal of Bone and Joint Surgery-American Volume 83A (2001) S151-S158.
[24] M.F. Swiontkowski, H.T. Aro, S. Donell, J.L. Esterhai, J. Goulet, A. Jones, P.J. Kregor, L. Nordsletten, G. Paiement, A. Patel, Recombinant human bone morphogenetic protein-2 in open tibial fractures - A subgroup analysis of data combined from two prospective randomized studies, Journal of Bone and Joint Surgery-American Volume 88A(6) (2006) 1258-1265.
[25] W. Sun, Z.R. Li, F.Q. Gao, Z.C. Shi, Q.D. Zhang, W.S. Guo, Recombinant Human Bone Morphogenetic Protein-2 in Debridement and Impacted Bone Graft for the Treatment of Femoral Head Osteonecrosis, Plos One 9(6) (2014) 6.
[26] M.D. McKee, Recombinant human bone morphogenic protein-7 - Applications for clinical trauma, Journal of Orthopaedic Trauma 19(10) (2005) S26-S28.
[27] N. Itasaki, S. Hoppler, Crosstalk Between Wnt and Bone Morphogenic Protein Signaling: A Turbulent Relationship, Developmental Dynamics 239(1) (2010) 16-33.
[28] Y. Chen, H.C. Whetstone, A. Youn, P. Nadesan, E.C.Y. Chow, A.C. Lin, B.A. Alman, beta-catenin signaling pathway is crucial for bone morphogenetic protein 2 to induce new bone formation, Journal of Biological Chemistry 282(1) (2007) 526-533.
[29] M. Zhang, Y. Yan, Y.B. Lim, D.Z. Tang, R. Xie, A. Chen, P. Tai, S.E. Harris, L.P. Xing, Y.X. Qin, D. Chen, BMP-2 Modulates beta-Catenin Signaling Through Stimulation of Lrp5 Expression and Inhibition of beta-TrCP Expression in Osteoblasts, Journal of Cellular Biochemistry 108(4) (2009) 896-905.
[30] L.J. Yang, K. Yamasaki, Y. Shirakata, X.J. Dai, S. Tokumaru, Y. Yahata, M. Tohyama, Y. Hanakawa, K. Sayama, K. Hashimoto, Bone morphogenetic protein-2 modulates Wnt and frizzled expression and enhances the canonical pathway of Wnt signaling in normal keratinocytes, Journal of Dermatological Science 42(2) (2006) 111-119.
[31] G.M. Boland, G. Perkins, D.J. Hall, R.S. Tuan, Wnt 3a promotes proliferation and suppresses osteogenic differentiation of adult human mesenchymal stem cells, Journal of Cellular Biochemistry 93(6) (2004) 1210-1230.
[32] K. Fujita, S. Janz, Attenuation of WNT signaling by DKK-1 and -2 regulates BMP2-induced osteoblast differentiation and expression of OPG, RANKL and M-CSF, Molecular Cancer 6 (2007).
[33] E.C. Rodríguez-Merchán, Bone Healing Materials in the Treatment of Recalcitrant Nonunions and Bone Defects, International Journal of Molecular Sciences 23(6) (2022) 3352.
[34] A.J. Salgado, O.P. Coutinho, R.L. Reis, Bone tissue engineering: state of the art and future trends, Macromolecular bioscience 4(8) (2004) 743-765.
[35] V. Karageorgiou, D. Kaplan, Porosity of 3D biomaterial scaffolds and osteogenesis, Biomaterials 26(27) (2005) 5474-5491.
[36] G. Wei, P.X. Ma, Structure and properties of nano-hydroxyapatite/polymer composite scaffolds for bone tissue engineering, Biomaterials 25(19) (2004) 4749-4757.

[37] L. Xia, K. Lin, X. Jiang, B. Fang, Y. Xu, J. Liu, D. Zeng, M. Zhang, X. Zhang, J. Chang, Effect of nano-structured bioceramic surface on osteogenic differentiation of adipose derived stem cells, Biomaterials 35(30) (2014) 8514-8527.
[38] H. Yanagida, M. Okada, M. Masuda, M. Ueki, I. Narama, S. Kitao, Y. Koyama, T. Furuzono, K. Takakuda, Cell adhesion and tissue response to hydroxyapatite nanocrystal-coated poly (L-lactic acid) fabric, Journal of bioscience and bioengineering 108(3) (2009) 235-243.
[39] K. Rezwan, Q.Z. Chen, J.J. Blaker, A.R. Boccaccini, Biodegradable and bioactive porous polymer/inorganic composite scaffolds for bone tissue engineering, Biomaterials 27(18) (2006) 3413-3431.
[40] A.H. Ambre, D.R. Katti, K.S. Katti, Biomineralized hydroxyapatite nanoclay composite scaffolds with polycaprolactone for stem cell-based bone tissue engineering, Journal of Biomedical Materials Research Part A 103(6) (2015) 2077-2101.
[41] A.H. Ambre, K.S. Katti, D.R. Katti, Nanoclay based composite scaffolds for bone tissue engineering applications, Journal of Nanotechnology in Engineering and Medicine 1(3) (2010) 031013.
[42] A. Ambre, K.S. Katti, D.R. Katti, In situ mineralized hydroxyapatite on amino acid modified nanoclays as novel bone biomaterials, Materials Science & Engineering C-Materials for Biological Applications 31(5) (2011) 1017-1029.
[43] A.H. Ambre, D.R. Katti, K.S. Katti, Nanoclays mediate stem cell differentiation and mineralized ECM formation on biopolymer scaffolds, Journal of Biomedical Materials Research Part A 101(9) (2013) 2644-2660.
[44] K. Kundu, D.R. Katti, K.S. Katti, Tissue-Engineered Interlocking Scaffold Blocks for the Regeneration of Bone, Jom 72(4) (2020) 1443-1457.
[45] R. Subbiah, A. Cheng, M.A. Ruehle, M.H. Hettiaratchi, L.E. Bertassoni, R.E. Guldberg, Effects of controlled dual growth factor delivery on bone regeneration following composite bone-muscle injury, Acta Biomaterialia 114 (2020) 63-75.
[46] P. Yilgor, R.A. Sousa, R.L. Reis, N. Hasirci, V. Hasirci, Effect of scaffold architecture and BMP-2/BMP-7 delivery on in vitro bone regeneration, Journal of Materials Science: Materials in Medicine 21(11) (2010) 2999-3008.
[47] K.S. Katti, D.R. Katti, A.H. Ambre, Asme, UNNATURAL AMINO ACIDS MODIFIED CLAYS FOR DESIGN OF SCAFFOLDS FOR BONE TISSUE ENGINEERING, Nemb2010: Proceedings of the Asme First Global Congress on Nanoengineering for Medicine and Biology - 2010 (2010) 227-228.
[48] K.S. Katti, A.H. Ambre, N. Peterka, D.R. Katti, Use of unnatural amino acids for design of novel organomodified clays as components of nanocomposite biomaterials, Philosophical Transactions of the Royal Society a-Mathematical Physical and Engineering Sciences 368(1917) (2010) 1963-1980.
[49] A.H. Ambre, D.R. Katti, K.S. Katti, Biomineralized hydroxyapatite nanoclay composite scaffolds with polycaprolactone for stem cell-based bone tissue engineering, Journal of Biomedical Materials Research - Part A (2015).
[50] K. Kundu, A. Afshar, D.R. Katti, M. Edirisinghe, K.S. Katti, Composite nanoclay-hydroxyapatite-polymer fiber scaffolds for bone tissue engineering manufactured using pressurized gyration, Composites Science and Technology 202 (2021) 108598.
[51] W.C. Oliver, G.M. Pharr, An improved technique for determining hardness and elastic modulus using load and displacement sensing indentation experiments, Journal of materials research 7(6) (1992) 1564-1583.
[52] M. Bouyer, R. Guillot, J. Lavaud, C. Plettinx, C. Olivier, V. Curry, J. Boutonnat, J.-L. Coll, F. Peyrin, V. Josserand, Surface delivery of tunable doses of BMP-2 from an adaptable polymeric scaffold induces volumetric bone regeneration, Biomaterials 104 (2016) 168-181.
[53] X.-L. Dong, W. Qi, W. Tao, L.-Y. Ma, C.-X. Fu, The dynamic behaviours of protein BMP-2 on hydroxyapatite nanoparticles, Molecular Simulation 37(13) (2011) 1097-1104.

[54] Y.-H. Kim, X. Yang, L. Shi, S.A. Lanham, J. Hilborn, R.O.C. Oreffo, D. Ossipov, J.I. Dawson, Bisphosphonate nanoclay edge-site interactions facilitate hydrogel self-assembly and sustained growth factor localization, Nature communications 11(1) (2020) 1-9.
[55] C. Scheufler, W. Sebald, M. Hülsmeyer, Crystal structure of human bone morphogenetic protein-2 at 2.7 Å resolution, Journal of molecular biology 287(1) (1999) 103-115.
[56] D.L. Griffith, P.C. Keck, T.K. Sampath, D.C. Rueger, W.D. Carlson, Three-dimensional structure of recombinant human osteogenic protein 1: Structural paradigm for the transforming growth factor beta superfamily, Proceedings of the National Academy of Sciences of the United States of America 93(2) (1996) 878-883.
[57] M.S. Rahman, N. Akhtar, H.M. Jamil, R.S. Banik, S.M. Asaduzzaman, TGF-β/BMP signaling and other molecular events: regulation of osteoblastogenesis and bone formation, Bone research 3(1) (2015) 1-20.
[58] T. Komori, Regulation of osteoblast differentiation by Runx2, Osteoimmunology, Springer2009, pp. 43-49.
[59] E.S. Sandhurst, S.V. Jaswandkar, K. Kundu, D.R. Katti, K.S. Katti, H. Sun, D. Engebretson, K.R. Francis, Nanoarchitectonics of a Microsphere-Based Scaffold for Modeling Neurodevelopment and Neurological Disease, ACS Applied Bio Materials (2022).
[60] A. Sharma, M.D.S. Molla, K.S. Katti, D.R. Katti, Multiscale models of degradation and healing of bone tissue engineering nanocomposite scaffolds, Journal of Nanomechanics and Micromechanics 7(4) (2017) 04017015.
[61] D. Sikdar, D. Katti, K. Katti, B. Mohanty, Effect of organic modifiers on dynamic and static nanomechanical properties and crystallinity of intercalated clay–polycaprolactam nanocomposites, Journal of applied polymer science 105(2) (2007) 790-802.
[62] C.X.F. Lam, M.M. Savalani, S.-H. Teoh, D.W. Hutmacher, Dynamics of in vitro polymer degradation of polycaprolactone-based scaffolds: accelerated versus simulated physiological conditions, Biomedical materials 3(3) (2008) 034108.
[63] W.D. Nix, H. Gao, Indentation size effects in crystalline materials: a law for strain gradient plasticity, Journal of the Mechanics and Physics of Solids 46(3) (1998) 411-425.
[64] A. Iost, R. Bigot, Indentation size effect: reality or artefact?, Journal of Materials Science 31(13) (1996) 3573-3577.
[65] M.F. Horstemeyer, M.I. Baskes, S.J. Plimpton, Length scale and time scale effects on the plastic flow of fcc metals, Acta Materialia 49(20) (2001) 4363-4374.
[66] M.V. Swain, Fracture Mechanics of Ceramics, Vol. 6, Edited by RC Bradt, AG Evans, FF Lange and DPH Hasselman, Plenum Press, New York (1983) 355-69.
[67] S.-Y. Tee, A. Bausch, P.A. Janmey, The mechanical cell, Current biology: CB 19(17) (2009) R745.
[68] R. Khanna, K.S. Katti, D.R. Katti, Experiments in nanomechanical properties of live osteoblast cells and cell–biomaterial interface, Journal of Nanotechnology in Engineering and Medicine 2(4) (2011).